Final Draft
of the original manuscript:

Galvao, T.L.P.; Kuznetsova, A.; Gomes, J.R.B.; Zheludkevich, M.L.; Tedim, J.; Ferreira, M.G.S.:

A computational UV–Vis spectroscopic study of the chemical speciation of 2-mercaptobenzothiazole corrosion inhibitor in aqueous solution

A Computational UV-Vis Spectroscopic Study of the Chemical Speciation of 2-Mercaptobenzothiazole Corrosion Inhibitor in Aqueous Solution

Tiago L. P. Galvão, Alena Kuznetsova, José R. B. Gomes, Mikhail L. Zheludkevich, João Tedim, Mário G. S. Ferreira

Tiago L. P. Galvão, Alena Kuznetsova, **João Tedim, Mário G. S. Ferreira**

CICECO-Aveiro Institute of Materials, Department of Materials and Ceramic Engineering, University of Aveiro, Campus Universitário de Santiago, 3810-193 Aveiro, Portugal

E-mail: tlpgalvao@ua.pt

José R. B. Gomes

CICECO-Aveiro Institute of Materials, Department of Chemistry, University of Aveiro, Campus Universitário de Santiago, 3810-193 Aveiro, Portugal

Mikhail L. Zheludkevich

Helmholtz-Zentrum Geesthacht, Centre for Materials and Coastal Research GmbH, Institute of Materials Research – MagIC, Max-Planck-Strasse 1, 21502 Geesthacht, Germany

Abstract In order to understand the chemical speciation of 2-mercaptobenzothiazole (MBT) corrosion inhibitor as a function of pH, the electronic absorption spectra was compared with those calculated at the EOM-CCSD, TD-M06-2X and TD-B3LYP levels of theory for several different species that may result from MBT reactions in aqueous solution. The computational spectroscopic analysis was supported by the energetics of tautomerization, deprotonation, non-covalent association and ion-pair formation reactions calculated at the M06-2X/6-31++G(d,p) level of theory. The thioketonic and deprotonated anionic forms of MBT were found to be the main species depending on the pH, while the formation of the ion-pair was also supported under basic conditions, especially when put in perspective of the release profiles of the inhibitor from nanocontainers published in the literature. The calculated energetic and electronic results were used to unveil the tautomeric, acid-base and ion-pair formation equilibrium, relevant to guide the application of MBT as a corrosion inhibitor, and establishing a foundation for future molecular modeling studies concerning the adsorption of MBT onto metal and metal alloys under different pHs.

1 Introduction

2-Mercaptobenzothiazole (MBT) is one of the most efficient and versatile organic corrosion inhibitors for several alloys used in the automotive, aeronautic and other industries. The nitrogen and sulfur high electron density atoms can act as adsorption centers to metals [1], favoring the formation of self-assembled protective layers [2].

However, the direct application of organic corrosion inhibitors in metal protective coatings might result in the decrease of their efficiency or quality [3, 4]. One solution, is the use of inert nanocontainers [4] capable of immobilizing the inhibitors and release them upon a local variation of the properties associated with corrosion (such as pH [5]) and/or degradation of the coating [4]. MBT in particular is one of the most common inhibitors for which this strategy has been employed [6–13].

The chemical speciation of MBT in aqueous solution (Figure 1) has a decisive influence on its release rate from nanocontainers and the type of adsorption onto the metal. The release of MBT from nanocontainers, under different trigger conditions of pH [9, 11–13] and NaCl concentration [9], has been rationalized in terms of acid-base equilibrium and the formation of the MBTNa ion-pair, respectively. In the case of the protection of the metal by MBT, the tautomeric and acid-base equilibria have been proposed to affect the formation of self-assembled monolayers [2, 14] and its inhibition efficiency [1, 7, 15, 16].

Besides being used as a corrosion inhibitor and a rubber vulcanization accelerator, MBT continues to find new applications due to its chelating ability [17–19]. For this reason, its structural properties are a matter of wide interest [1, 20]. In our research group, MBT was recently investigated concerning its photodegradation mechanism [21]. Due to its importance to understand the corrosion inhibition mechanism of different active metals after the release of inhibitors from supramolecular containers, the tautomeric, acid-base and ion-pair equilibria (Figure 1) in aqueous solution as a function of pH and in the presence of NaCl, will be

3

investigated considering a combined UV-Vis electronic absorption, computational spectroscopic (EOM-CCSD, TD-M06-2X and TD-B3LYP) and energetic (M06-2X) study.
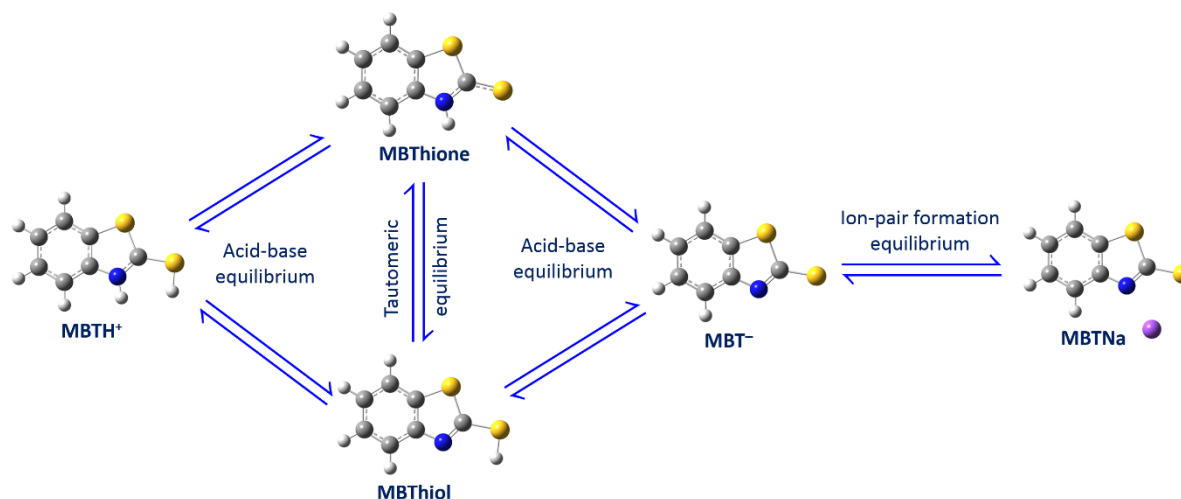

Fig. 1 Different MBT structures and equilibria studied in this work. Color code for spheres: grey is carbon; white is hydrogen; blue is nitrogen, yellow is sulfur; and purple is sodium. Equations are unbalanced on purpose.

The chemical speciation of MBT in solution is a major challenge to find its ideal application conditions [1, 20, 22–26]. The present work aims to render insights on the structure of MBT under favorable conditions for the occurrence of corrosion, which is fundamental to understand the chemisorption or physisorption of MBT onto metals, the formation of self-assembled protective multilayers, and its release from supramolecular containers [4].

2 UV-Vis Electronic Spectroscopy Details

All the chemicals were obtained from Sigma-Aldrich with a minimum purity degree of 98 % and used without any further purification.

A $2 \cdot 10^{-2}$ M MBT solution was prepared by dissolution of MBT powder in $2 \cdot 10^{-2}$ M NaOH under vigorous stirring until total dissolution of MBT in NaOH solution. Afterwards, a $4 \cdot 10^{-5}$ M MBT solution was prepared after dilution of the $2 \cdot 10^{-2}$ M MBT solution with deionized water and stored in the absence of light. The pH of aliquots of the $4 \cdot 10^{-5}$ M MBT solution was changed by the addition of drops of $5 \cdot 10^{-2}$ M NaOH or $5 \cdot 10^{-2}$ M HNO_3. Absorbance values were immediately collected after the preparation of the solutions in order to minimize the influence of any other external effects besides the influence of pH.

UV-Vis electronic absorption spectra of MBT solutions of different stable pHs were collected using a Sarspec SPEC SPEED+ UV/Vis with a quartz cuvette (l = 1 cm) and deionized water as a background reference.

Three independent replicates of this procedure were performed, one being presented during the discussion of the results and another two in the Supplementary Material.

All the pH values measured in this work were controlled using a HACH HQ40d Portable pH-meter with an IntelliCAL™ PHC101 standard gel filled pH electrode in the pH range between 2 and 11.

3 Computational Details

All the computational calculations reported in this work were performed using the Gaussian 09 code [27].

The molecular structures of MBT and its derivatives used for the simulation of the absorption spectra, calculation of association energies and logarithmic acid dissociation constants were optimized using density functional theory (DFT) with the hybrid functional of Truhlar and Zhao (M06-2X) [28] and the 6-31++G(d,p) basis set. The structures were characterized as true minima on the potential energy surface from a vibrational frequencies analysis in which imaginary modes were absent. The vibrational frequencies calculations

were also used to obtain the thermal corrections to enthalpies and Gibbs free energies of association and deprotonation reactions, at $T = 298.15$ K.

To implicitly simulate the influence of water, the Polarizable Continuum Model (PCM) [29] as a self-consistent reaction field (SCRF) was used for the calculation of equilibrium geometries, vibrational frequencies, association energies, excited state calculations and logarithmic acid dissociation constants. For comparison with experimental logarithmic acid dissociation constants, dimethyl sulfoxide (DMSO) was also used as implicit solvent.

After the M06-2X/6-31++G(d,p) optimization step, three methods were used to predict the absorption spectra of MBT through the calculation of excited state single point energy calculations. Since the geometry of the excited state was assumed to be the same as the fundamental state, the theoretical excitation energies and oscillator strengths calculated correspond to vertical transitions. The methods used were the time-dependent [30] density functional theory with the hybrid B3LYP [31] and M06-2X [28] functionals (TD-B3LYP and TD-M06-2X, respectively), both solved for twenty states, and the equation of motion coupled cluster singles and doubles (EOM-CCSD) theoretical method [32, 33], which was solved for fifteen states. Atomic electronic densities were described with the 6-31++G(d,p) basis set. The EOM-CCSD method was chosen because it was suggested to be able to provide accurate excitation energies [34] and oscillator strengths [35] that can be used to interpret the positions and intensities, respectively, of the experimental UV-Vis absorption bands. Caricato has also shown that the EOM-CCSD method can be efficiently applied together with the PCM method (EOM-CCSD-PCM), to simulate the polarization effects of the solvent, allowing to obtain excitation energies that follow the experimental trends [36]. While EOM-CCSD calculations are computationally feasible for small molecules, such computations become rapidly very expensive for larger systems. So, for comparison purposes, the TD-DFT methods were also chosen because they are less expensive than the EOM-CCSD and can be interesting alternatives for the study of larger molecules.

The association enthalpies and Gibbs energies calculated at the M06-2X/6-31++G(d,p) level of theory were corrected for basis set superposition error with the counterpoise method [37, 38]. Since the Gaussian 09 code [27] does not allow to use the counterpoise correction together with the PCM method, a two-step methodology was used. In the first step, geometry optimization and vibrational frequencies calculation were performed within the SCRF formalism and, in the second step, the counterpoise correction was calculated without the considering the PCM method (gas-phase calculation) using the geometry optimized in the previous step. In the case of the most stable conformation of MBTNa, the association enthalpies and Gibbs energies were also obtained using the PCM method together with a correction for basis set superposition error (BSSE) by calculating the energy of each fragment in the presence of ghost functions of the other fragment (MBT^- in the presence of ghost functions of Na^+, and Na^+ in the presence of ghost functions of MBT^-).

Logarithmic acid dissociation constants (pK_a) were calculated considering a thermodynamic cycle described in detail elsewhere [39], which is based on the reaction described by equation (1), where AH represents an acid (MBT, 1H-benzimidazole, 1,3-benzothiazole, benzo-1,2,3-triazole, indole, thiophenol, 1,2-benzisothiazol-3(2H)-one or 1,2-benzoxazolin-2(3H)-one) and A^- the respective conjugate base. From the computational Gibbs energies in the gaseous phase and the respective solvation energies calculated with the M06-2X/6-31++G(d,p)/PCM method, equation (2) was used to obtain the deprotonation Gibbs energy in the aqueous phase for reaction (1), $\Delta G(aq)$. Since the $G(g)$ standard state is 1 atm and the standard state for the solvation energies is 1M, $G(g)$ values were converted to 1 M using equation (3) and considering that the molar volume occupied by an ideal gas at 298.15 K and 1 atm is $V_m = 24.46$ dm^3. Assuming $\Delta G(aq) = \Delta G°$, it was possible to calculate the pK_a values according to equation (4). In the case of H^+, the Gibbs energy in the gaseous phase, $G(g) = -26.28$ kJ·mol^{-1}, was calculated using the Sackur-Tetrode equation [40], and for the Gibbs energy of solvation, the experimental value $G(solv) = -1104.58$ kJ·mol^{-1} [39,

41] was used. Considering the methodology described above, equation (5) was deduced [39], and the pK$_a$ constants were calculated.

$$AH \rightleftharpoons A^- + H^+ \tag{1}$$

$$\Delta G(aq) = G(A^-(g)) + G_{solv}(A^-) + G(H^+(g)) + G_{solv}(H^+) - G(AH(g)) - G_{solv}(AH) \tag{2}$$

$$G(1 \text{ mol·L}^{-1}, 298.15 \text{ K}) = G(1 \text{ atm}, 298.15 \text{ K}) + RT \ln V_m \tag{3}$$

$$pK_a = \frac{\Delta G°}{RT \ln(10)} \tag{4}$$

$$pK_a = \frac{\left[G(A^-(g)) + G_{solv}(A^-(g)) - G(AH(g)) - G_{solv}(AH(g)) - 1130.85 \right]}{RT \ln(10)} \tag{5}$$

4 Electronic Absorption Results

Figure 2 presents the UV-Vis spectra of MBT aqueous solutions (4 · 10^{-5} M) with different pH values. The UV-Vis spectra reveal that MBT possesses two absorption bands, one with maximum absorbance at the wavelength range of 230-240 nm (peak A) and a second at 308-320 nm (peak B). The main features of these spectra are that for pH higher than 7 the maximum absorbance of peak B shifts to lower wavelengths, and is more intense in comparison with peak A for all the considered pH values. Two other independent replicates of the UV-Vis spectra, in good agreement with those presented in Figure 2, can be found in the Supplementary Material.
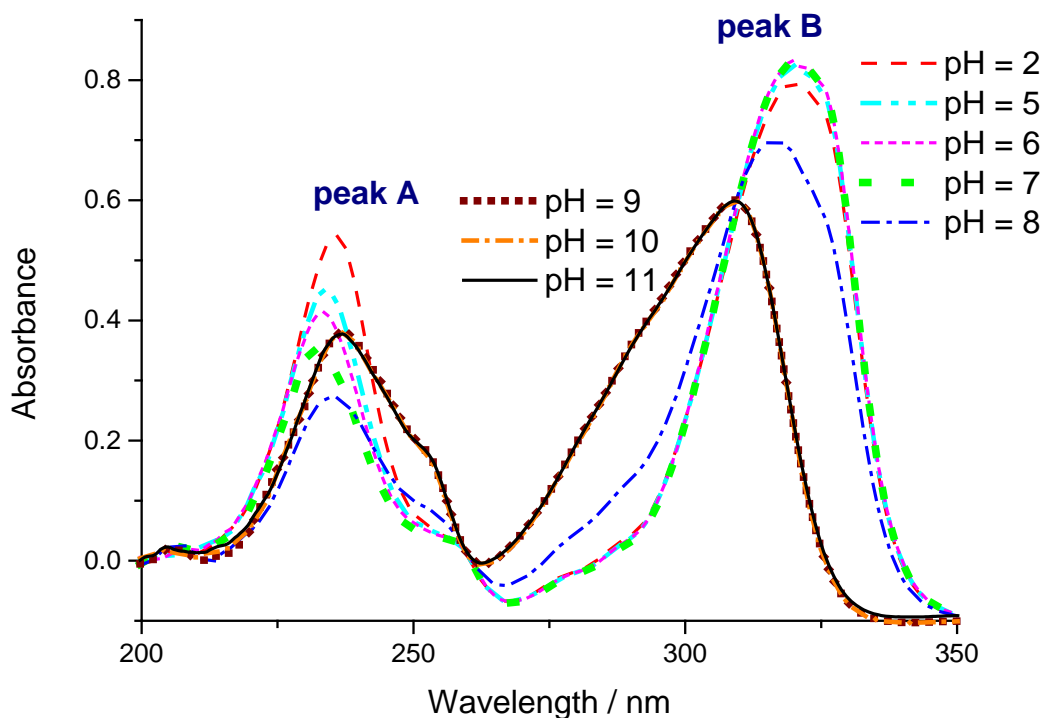
Fig. 2 Experimental UV-Vis spectra of MBT $4 \cdot 10^{-5}$ M obtained at different pH values.

The absorbance of peak A decreases from pH 2 to pH 8, reaching its lowest value. From pH 8 to pH 9 it is seen an increase of the absorbance of this peak. For pH values higher than 9, the absorbance remains nearly constant until pH 11.

In the case of peak B it is observed that the absorbance is almost constant between pH 2 and pH 7. For pH values higher than 7, the absorbance of peak B diminishes until pH 9. Above pH 9 and up to pH 11, the absorbance of peak B stays unaltered.

5 Discussion

5.1 Tautomeric equilibrium in the crystalline phase

Identifying the existing tautomeric form of MBT in the crystalline phase is identifying the tautomeric form that exists in the starting material used in this study and, also, the favored tautomeric form under conditions with the strongest degree of non-covalent interactions between the molecules through hydrogen bonding and $\pi\cdots\pi$ staking, such as in a MBT protective film on top of a metal [2, 14].

In order to make this identification, bond lengths of the optimized structures of MBThiol and MBThione at the M06-2X/6-31++G(d,p) level of theory were compared with those obtained from crystallographic structures reported in the literature [42, 43] (Figure 3). The probability ellipsoids of the electronic density of the hydrogens was not determined experimentally [42, 43] and, for this reason, the favored tautomeric form in the crystalline phase is not clearly known.

The experimental bond lengths for the crystalline phase and those calculated with the M06-2X approach for MBThiol and MBThione are presented in Figure S3 of the Supplementary Material. From the agreement between the bond lengths obtained for MBThione and those obtained experimentally for the crystalline phase, particularly for the C–N and C–S bonds, is possible to conclude that this is the form that exists in the crystal and, probably, in the case of the formation of a protective film over certain metallic surfaces where intermolecular interactions between the molecules also play a fundamental role [2]. This conclusion is supported by the energetic results presented in Figure 3, which show that MBThione has more favorable hydrogen bonding and $\pi\cdots\pi$ stacking interactions, which particularly in the case of the hydrogen-bonded dimers resemble those existent in the

crystalline structure [42, 43]. These results also show that the equilibrium for the reaction of conversion between the associated tautomers is displaced towards MBThione.
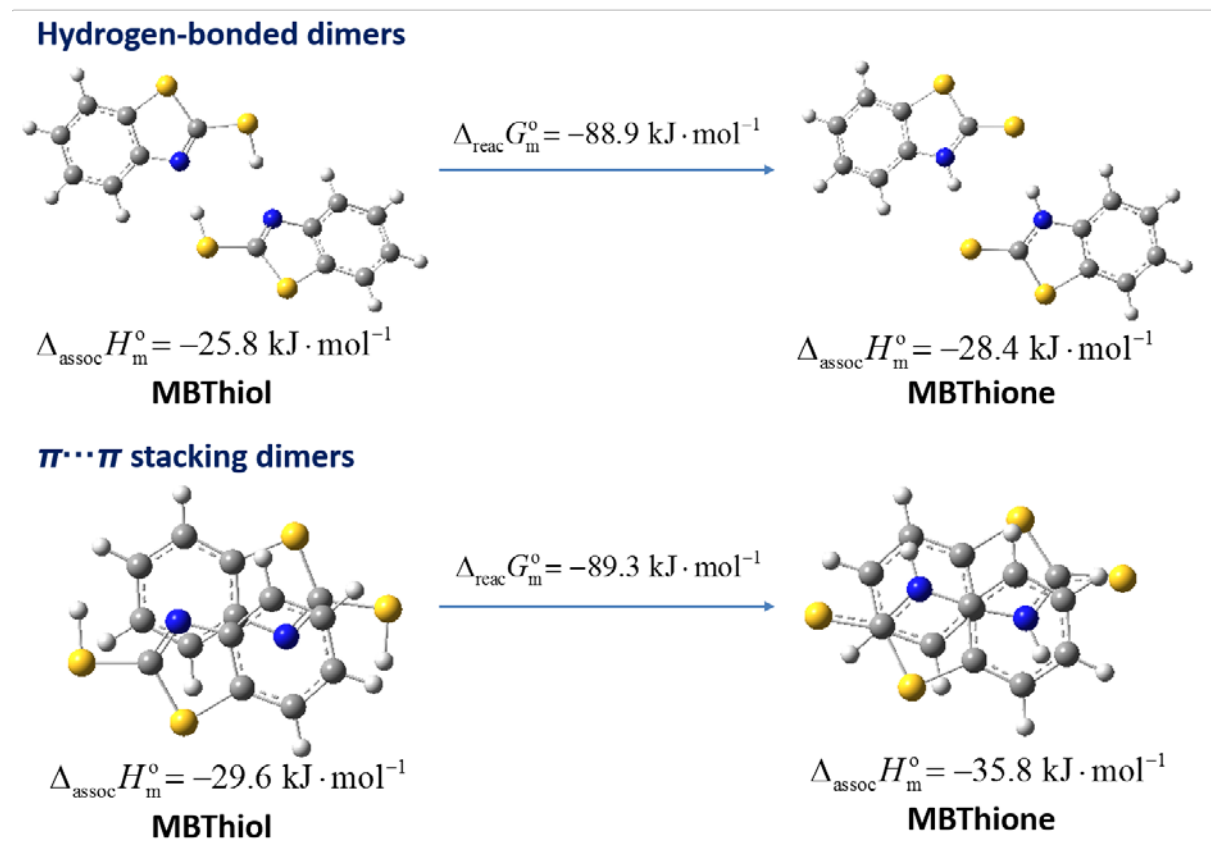

Fig. 3 Enthalpies of association of MBThiol and MBThione and Gibbs energies for the reaction of conversion between both tautomeric structures, at $T = 298.15$ K. Color code as in Figure 1.

5.2 Tautomeric equilibrium in solution under near neutral conditions

In order to interpret the experimental UV-Vis spectra obtained for several pH values (Figure 2), the absorption spectra of different MBT species were simulated computationally at the EOM-CCSD/6-31++G(d,p), TD-M06-2X/6-31++G(d,p) and TD-B3LYP/6-31++G(d,p) levels

of theory (Table 1 and Figure 4). Molecular orbitals responsible for these transitions are represented in Figure S4 of the Supplementary Material.

Table 1 Relevant excitation energies and oscillator strengths for different MBT species calculated at the EOM-CCSD/6-31++g(d,p), TD-B3LYP/6-31++g(d,p) and TD-M06-2X/6-31++g(d,p) levels of theory.

| Species	Method	Wavelength / nm (oscillator strength)	
		Peak A	Peak B
MBThiol	EOM-CCSD	196 (0.42); 207 (0.16); 228 (0.36)	---
	TD-B3LYP	220 (0.40)	262 (0.22), 268 (0.23)
	TD-M06-2X	207 (0.50), 214 (0.21)	243 (0.28), 251 (0.21)
MBThione	EOM-CCSD	203 (0.34)	291 (0.48)
	TD-B3LYP	220 (0.11); 222 (0.12); 250 (0.11)	303 (0.51)
	TD-M06-2X	215 (0.26), 226 (0.13)	293 (0.54)
MBT^-	EOM-CCSD	207 (0.29); 218 (0.25)	278 (0.43)
	TD-B3LYP	233 (0.27); 245 (0.12)	308 (0.50)
	TD-M06-2X	216 (0.31), 228 (0.29)	289 (0.53)
MBTNa	EOM-CCSD	206 (0.28); 217 (0.24)	277 (0.42)
	TD-B3LYP	228 (0.21); 239 (0.13)	305 (0.51)
	TD-M06-2X	214 (0.21), 221 (0.25), 229 (0.16)	287 (0.52)
$MBTH^+$	EOM-CCSD	191 (0.19)	242 (0.26); 266 (0.24)
	TD-B3LYP	219 (0.23)	284 (0.22); 290 (0.25)
	TD-M06-2X	200 (0.28)	270 (0.42)
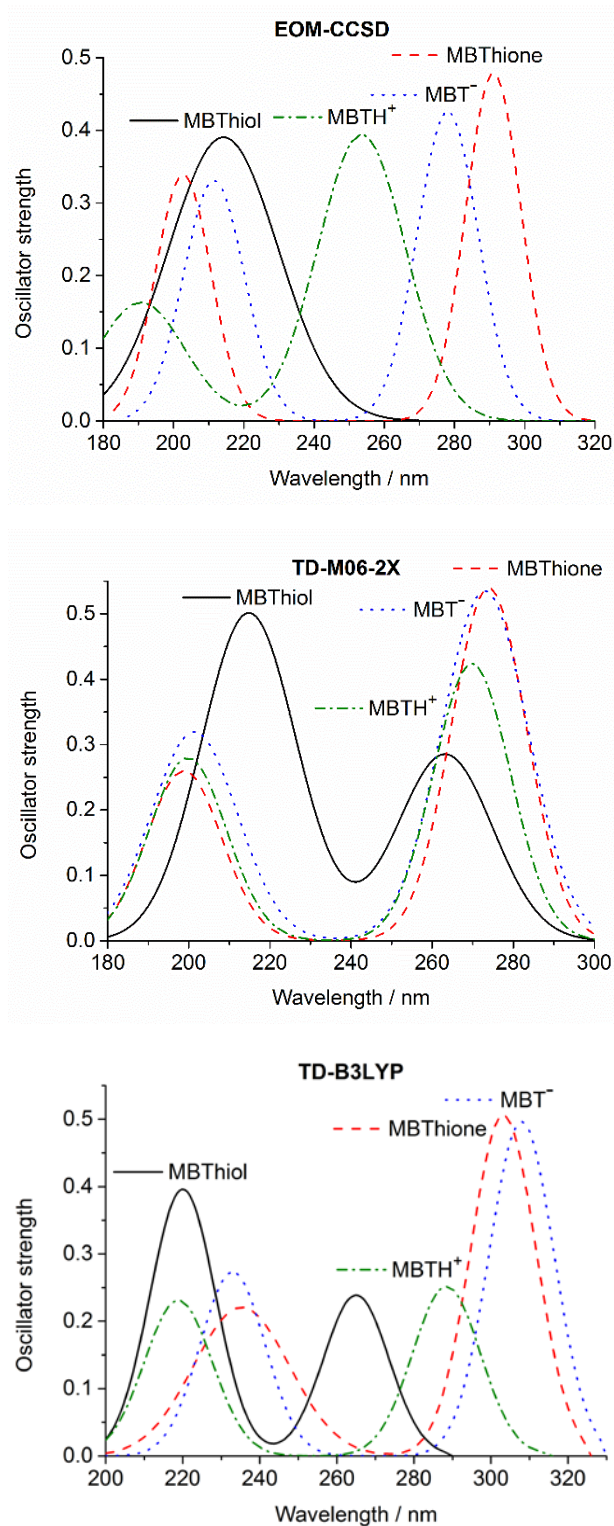
Fig. 4 Theoretical UV-Vis spectra for different MBT species.

The tautomeric equilibrium between MBThiol and MBThione and the possible protonation and deprotonation of these species to form MBTH$^+$ or MBT$^-$, under acidic and basic conditions, respectively, were taken into account. In the case of MBThiol, only the *cis*

13

conformation (with the S−H bond directed to the C−N bond) was considered, since it is more stable than the *trans* conformation, according to the results presented in Figure 5.
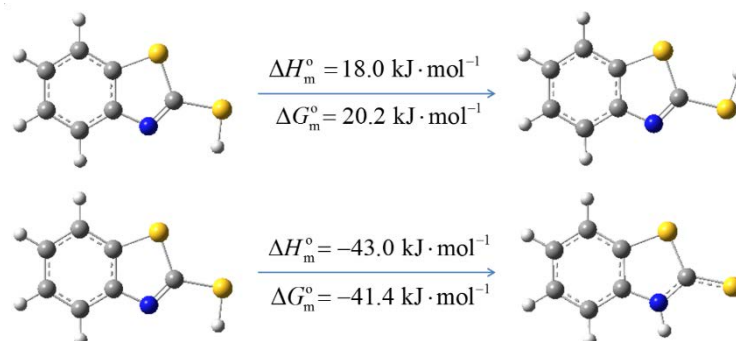

Fig. 5 Computational enthalpies and Gibbs energies, at $T = 298.15$ K, between the *cis* and *trans* conformations of MBThiol (above), and between MBThiol and MBThione (below). Color code as in Figure 1.

Comparing the experimental and computational wavelengths, under neutral conditions, peak A can be attributed to MBThiol or to MBThione, whereas, peak B can only be attributed to MBThione. According to the experimental UV-Vis spectra (Figure 2), peak B is always more intense than peak A. This attribution is in agreement with the theoretical peak B of MBThione having a higher oscillator strength in comparison with peak A of MBThiol or MBThione.

In order to verify to which tautomeric form (MBThiol or MBThione) can be attributed the peak A of the experimental UV-Vis, their pK$_a$'s were also computed as described in the Computational Details section. The accuracy of the results obtained was analyzed comparing the theoretical pK$_a$'s with experimental values available in literature for compounds with similar structural features (1*H*-benzimidazole [44], 1,3-benzothiazole [44], benzo-1,2,3-triazole [44, 45], índole [44, 46], thiophenol [47], 1,2-benzisothiazol-3(2*H*)-one [48] and 1,2-benzoxazolin-2(3*H*)-one [48]). From the nine pK$_a$ values available in literature and presented in Table S2 of the Supplementary Material it is found that the mean absolute deviation

between the experimental and computational results is 1.6, whereas the mean deviation is −0.4, which shows that the computational approach is suitable for calculating pK_a values of this kind of organic compounds, thus supporting the use of the calculated data for the interpretation of the UV-Vis spectra.

The pK_a value of MBThiol reported in Table 2 is too low for this form to exist in equilibrium with MBThione at neutral and near neutral pH, thus making it unlikely for this species to describe peak A. For example, considering equation (6), where A^- and AH correspond to the deprotonated anionic form and the neutral form, respectively, for pH = 7, taking into account only the pK_a of MBThiol, the molar percentages of MBThiol and MBT^- would be 0.0 % and 100.0 %, respectively. Moreover, the difference between the Gibbs energies of MBThiol and MBThione (Figure 5) also confirms this conclusion, since according to equation (7), where $G_m^\circ(i)$ is the computed Gibbs energy in the aqueous phase of each tautomer at T = 298.15 K, MBT exists only as MBThione (x_i(MBThione) ≈ 100.0 %, x_i(MBThiol) ≈ 0.0 %).

$$\frac{[A^-]}{[AH]} = 10^{pH-pK_a} \tag{6}$$

$$x_i = \frac{e^{-\left[\frac{G_m^\circ(i)}{RT}\right]}}{\sum_{i=1}^{n} e^{-\left[\frac{G_m^\circ(i)}{RT}\right]}} \times 100 \tag{7}$$

Table 2 Experimental (exp.) and calculated (calc.) pK_a values of MBT.

pK_a(exp.)	pK_a(MBThiol) (Δ(exp.− calc.))	pK_a(MBThione) (Δ(exp.− calc.))
6.95 [24]	−0.6 (+7.55)	6.7 (+0.25)
7.86 [25]	−0.6 (+8.46)	6.7 (+1.16)

| 7.49 [26] | −0.6 (+8.09) | 6.7 (+0.79) |
| 10.90 [26] | −0.6 (+11.5) | 6.7 (+4.2) |

5.3 Acid-base equilibrium under basic conditions

At basic pH peak B presents a slightly lower absorption wavelength than in the cases of acidic and neutral pHs (Figure 1), which is in agreement with the lower EOM-CCSD and TD-M06-2X absorption wavelength of peak B observed for MBT⁻ than for MBThione (Table 1 and Figure 3). It should be noted that only EOM-CCSD and TD-M06-2X seem able to predict this subtle decrease of the wavelength, being more clearly noticed in the case of the more accurate description of the wavefunction, EOM-CCSD. In fact, by comparing the TD-B3LYP with the TD-M06-2X and EOM-CCSD results for MBT⁻ and MBThione (Table 1), it is seen that the former approach provides an opposite variation to that obtained by the other two. The computed oscillator strength for peak B decreases from MBThione to MBT⁻ (Table 1 and Figure 3), which is also in agreement with a lower absorbance of the experimental peak B for pH > 7 in comparison with absorbance values at acidic and neutral pHs (Figure 1). It is also worth mentioning that this decrease of intensity from MBThione to MBT⁻ is also more notorious in the case of the EOM-CCSD method. The qualitative agreement between the experimental and calculated trends of the position and relative intensities of the peaks allow to attribute MBT⁻ as being responsible for the observed peaks for pH > 7, whereas at acidic and neutral pHs the importance of MBThione should increase, depending on the pK_a value of MBT.

Considering equation (6) and the calculated pK_a reported in Table 2 for MBThione, it is possible to conclude that the UV-Vis spectra at near neutral conditions correspond to the neutral molecule (MBThione) in equilibrium with the deprotonated anionic form, whereas for

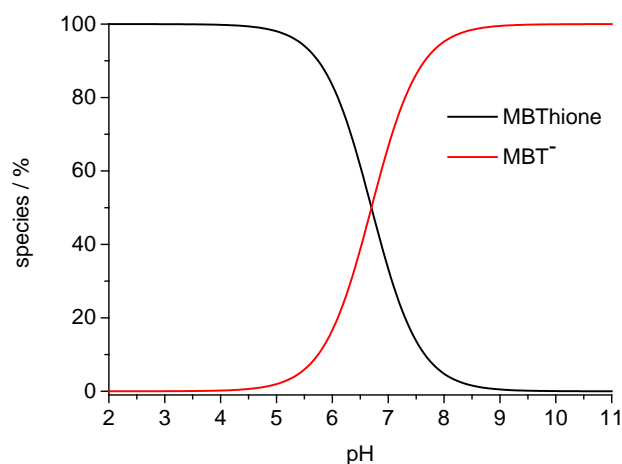pH > 8 it can be attributed mainly to MBT⁻, as can be verified by the molar percentages presented in Figure 6.

Fig. 6 Molar percentages of MBThione and MBT⁻ as a function of pH.

Furthermore, the calculated pK_a for MBThione is very similar to that obtained by Malouki *et al.* [24], which allows to mutually validate our analysis and recommend their value as the most likely pK_a for this compound.

5.4 Tautomeric and acid-base equilibrium under acidic conditions

As for the presence of MBThiol at very acidic pH, the TD-B3LYP and TD-M06-2X calculations predict a shift of both peaks of MBThiol to lower wavelengths in comparison with MBThione (which is the main species at neutral and near neutral pHs as shown above), whereas the EOM-CCSD results predict the existence of only peak A for MBThiol (Figure 3), which is not the case when observing the experimental UV-Vis spectra (Figure 1). As a result, even at pH = 2, the absorption bands obtained experimentally do not correspond to MBThiol and therefore MBThione is still the favored tautomeric species.

To find out if MBTH$^+$ can be the predominant form at pH = 2, the UV-Vis spectra of MBTH$^+$ was also simulated theoretically. The simulated spectra with the three methods show that both peaks A and B of MBTH$^+$ appear at significant lower wavelengths than those of MBThione, which is not the case when comparing the experimental absorption spectra at pH = 2 with the absorption spectra at near neutral pH. As a result, the protonation of MBThione to form MBTH$^+$ at very acidic pH is not likely to occur in the pH range examined in this study (pH = [2,11]).

5.5 Formation of MBTNa

Another factor that might influence the experimental UV-Vis spectra under basic conditions is the formation of an ion-pair between deprotonated MBT and the sodium cation resulting from the base (NaOH) added to the solution. To find out if this association would be favorable, the interaction energies between MBT$^-$ and Na$^+$ were calculated at the M06-2X/6-31++G(d,p)/PCM level of theory and corrected for BSSE. For comparison, the association between neutral MBT and Na$^+$ was also analyzed. According to the results presented in Figure 7, the association of Na$^+$ with MBT$^-$ is more favorable than with MBThione and MBThiol. There is also one conformation of MBT$^-$·Na$^+$ (conformation I) for which the enthalpy of association is very favorable and large enough to overcome the translational and rotational entropic penalty [49] arising from the formation of the ion-pair, resulting in a negative Gibbs reaction energy. The favorable association obtained for conformation I of MBT$^-$·Na$^+$ was confirmed by two different methods of taking into account implicit solvation effects and correction for BSSE, as described in the Computational Results section. Moreover, the association between MBT$^-$ and Na$^+$ seems large enough in terms of enthalpy and Gibbs energy to be more extensive than the interaction of MBT$^-$ with one water molecule.

According to the theoretical absorbance results (Table 1), the calculated excitation energies and intensities for MBTNa are nearly the same as for MBT⁻. For this reason, the UV-Vis spectra obtained for pH > 7 using NaOH as a base, might also be attributed to MBTNa.

During the analysis of the release profiles of MBT from nanocontainers based on silica nanocapsules [9] in NaCl aqueous solutions, it was verified that as the concentration of NaCl increased, the extent and rate of MBT release from the nanocontainers also increased. Since ionic exchange is not known to be a driving force for the release of molecules from this type of containers, this result was previously interpreted [9] in terms of the formation of MBTNa, which is known to be more soluble than neutral MBT [50]. The present energetic and spectroscopic analysis also supports this assumption, and the ability of Na⁺ to have some degree of association with MBT⁻ has also been verified by other authors [51].
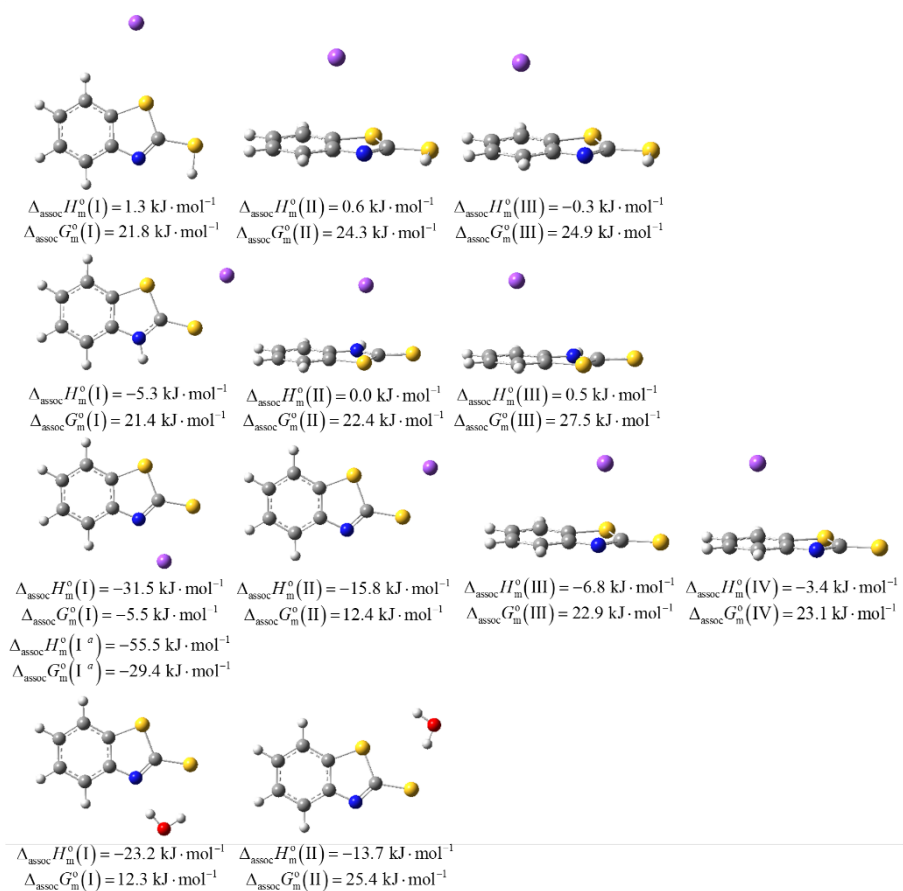

Fig. 7 Thermodynamic results at $T = 298.15$ K for the association between MBThiol and Na⁺ (first row), MBThione and Na⁺ (second row), MBT⁻ and Na⁺ (third row) and between MBT⁻ and H_2O (fourth row), calculated at the M06-2X/6-31++G(d,p)/PCM level of theory corrected

with counterpoise (the results identified with 'ᵃ' were corrected for BSSE using ghost functions as described in the Computational Details). Red is oxygen and the remaining colors are as in Figure 1.

5.6 Simulation of the UV-Vis electronic spectra

Taking into account the results discussed above and based on the predicted UV-Vis spectra for MBThione and MBT⁻ together with the molar percentages of both forms as a function of pH, calculated using the experimental pK_a value [24] validated in this study, the spectra of MBT was predicted considering the EOM-CCSD method, since it represents more accurately the majority of the features essential to understand the experimental UV-Vis spectra. The obtained spectra presented in Figure 8 resemble the most noticeable features of the experimental UV-Vis presented in Figure 2, particularly: i) peak A is more intense for very acidic pH than for very basic pH, passing throw a minimum at near neutral pH; ii) peak A is shifted to higher wavelengths as the pH increases, although the degree of this shift is smaller in the experimental spectra; iii) peak B is more intense for acidic pH than for basic pH; and iv) peak B exhibits a shift to lower wavelengths as the pH increases.

The similarity between the experimental and simulated spectra supports that, in aqueous solution, MBT exists in equilibrium mainly between MBThione and MBT⁻ (and between MBT⁻ and Na^+ as verified above) depending on the pH of the solution, which has direct implications on the corrosion inhibition mechanism of metals [7].
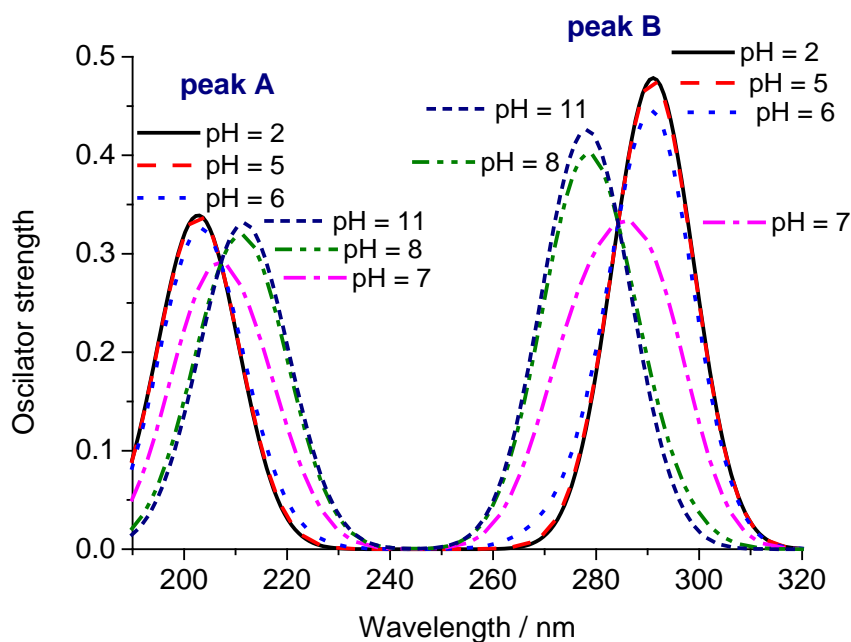
Fig. 8 Predicted UV-Vis spectra of MBT at the EOM-CCSD/6-31++g(d,p) level of theory, considering the relative populations of MBThione and MBT⁻ as a function of pH.

Based on the discussion above, the chemical speciation of MBT, in aqueous solution as a function of pH and also in the crystalline phase, is summarized in Figure 9. As it can be seen, MBThione is favored at acidic and near neutral pH while isolated or sodium complexed MBT⁻ species are favored at higher pH values.
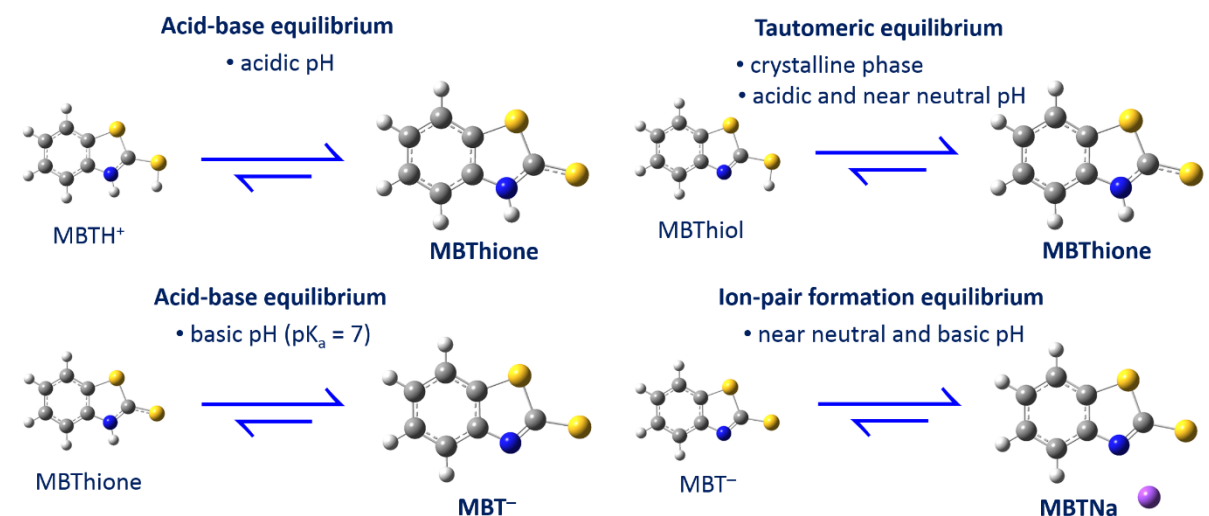
Fig. 9 Favored species resulting from the acid-base, tautomeric and ion-pair formation equilibrium involving MBT. Color code as in Figure 1. Notice that equations are unbalanced on purpose.

6 Conclusions

In this study the tautomeric, acid-base and ion-pair formation equilibria were investigated by comparing the UV-Vis electronic absorption spectra obtained for several pHs with the electronic transitions calculated computationally at the EOM-CCSD/6-31++G(d,p)/PCM, TD-M06-2X/6-31++G(d,p)/PCM and TD-B3LYP/6-31++G(d,p)/PCM levels of theory for different MBT species, which allowed to conclude that the EOM-CCSD method reproduces all the features of the obtained electronic absorption spectra, while the TD-M06-2X is also able to predict most aspects of the spectra, hence offering a good compromise between accuracy and computational cost. The spectroscopic study was supported by the calculation of the enthalpies and Gibbs energies of tautomerization, deprotonation, association and ion-pair formation reactions using the M06-2X/6-31++G(d,p) computational method. The identification of the main MBT species allowed to clarify several contradictory reports in literature regarding its tautomeric and acid-base equilibria, making possible to optimize its application conditions, as well as to establish a foundation for future molecular modeling adsorption studies dealing with the inhibition efficiency of MBT.

References

1. Gholami M, Danaee I, Maddahy MH, RashvandAvei M (2013) Correlated ab Initio and Electroanalytical Study on Inhibition Behavior of 2-Mercaptobenzothiazole and Its Thiole–Thione Tautomerism Effect for the Corrosion of Steel (API 5L X52) in Sulphuric Acid Solution. Ind Eng Chem Res 52:14875–14889. doi: 10.1021/ie402108g

2. Shervedani RK, Hatefi-Mehrjardi A, Babadi MK (2007) Comparative electrochemical study of self-assembled monolayers of 2-mercaptobenzoxazole, 2-mercaptobenzothiazole, and 2-mercaptobenzimidazole formed on polycrystalline gold electrode. Electrochim Acta 52:7051–7060. doi: 10.1016/j.electacta.2007.05.030

3. Shchukin DG, Zheludkevich M, Yasakau K, et al. (2006) Layer-by-Layer Assembled Nanocontainers for Self-Healing Corrosion Protection. Adv Mater 18:1672–1678. doi: 10.1002/adma.200502053

4. Zheludkevich ML, Tedim J, Ferreira MGS (2012) "Smart" coatings for active corrosion protection based on multi-functional micro and nanocontainers. Electrochim Acta 82:314–323. doi: 10.1016/j.electacta.2012.04.095

5. Bastos AC, Karavai O V., Zheludkevich ML, et al. (2010) Localised measurements of pH and dissolved oxygen as complements to SVET in the investigation of corrosion at defects in coated aluminum alloy. Electroanalysis 22:2009–2016. doi: 10.1002/elan.201000076

6. Shchukin DG, Lamaka S V., Yasakau KA, et al. (2008) Active anticorrosion coatings with halloysite nanocontainers. J Phys Chem C 112:958–964. doi: 10.1021/jp076188r

7. Poznyak SK, Tedim J, Rodrigues LM, et al. (2009) Novel inorganic host layered double hydroxides intercalated with guest organic inhibitors for anticorrosion applications. ACS Appl Mater Interfaces 1:2353–2362. doi: 10.1021/am900495r

8. Tedim J, Poznyak SK, Kuznetsova A, et al. (2010) Enhancement of Active Corrosion Protection via Combination of Inhibitor-Loaded Nanocontainers. ACS Appl Mater Interfaces 2:1528–1535. doi: 10.1021/am100174t

9. Maia F, Tedim J, Lisenkov AD, et al. (2012) Silica nanocontainers for active corrosion protection. Nanoscale 4:1287. doi: 10.1039/c2nr11536k

10. Abdullayev E, Abbasov V, Tursunbayeva A, et al. (2013) Self-healing coatings based on halloysite clay polymer composites for protection of copper alloys. ACS Appl Mater Interfaces 5:4464–4471. doi: 10.1021/am400936m

11. Borisova D, Akçakayiran D, Schenderlein M, et al. (2013) Nanocontainer-based anticorrosive coatings: Effect of the container size on the self-healing performance. Adv Funct Mater 23:3799–3812. doi: 10.1002/adfm.201203715

12. Lv LP, Landfester K, Crespy D (2014) Stimuli-selective delivery of two payloads from dual responsive nanocontainers. Chem Mater 26:3351–3353. doi: 10.1021/cm500923d

13. Carneiro J, Caetano AF, Kuznetsova A, et al. (2015) Polyelectrolyte-modified layered double hydroxide nanocontainers as vehicles for combined inhibitors. RSC Adv 5:39916–39929. doi: 10.1039/C5RA03741G

14. Jun YY, Beng KS (2004) Electrochemical study of monolayers of heterocyclic thiols self-assembled on polycrystalline gold electrode: The effect of solution pH on redox kinetics. Electrochem commun 6:87–90. doi: 10.1016/j.elecom.2003.10.023

15. Breedon M, Per MC, Cole IS, Barnard AS (2014) Molecular ionization and deprotonation energies as indicators of functional coating performance. J Mater Chem A 2:16660–16668. doi: 10.1039/C4TA03414G

16. Winkler DA, Breedon M, Hughes a. E, et al. (2014) Towards chromate-free corrosion inhibitors: structure–property models for organic alternatives. Green Chem 16:3349. doi: 10.1039/c3gc42540a

17. Rajasekharan-Nair R, Moore D, Kennedy AR, et al. (2014) The stability of mercaptobenzothiazole based soft scorpionate complexes. Inorg Chem 53:10276–82. doi: 10.1021/ic5013236

18. Herrera Cano N, Ballari MS, López AG, Santiago AN (2015) New Synthesis and Biological Evaluation of Benzothiazole Derivates as Antifungal Agents. J Agric Food Chem 63:3681–3686. doi: 10.1021/acs.jafc.5b00150

19. Ilichev VA, Pushkarev AP, Rumyantcev R V., et al. (2015) Luminescent properties of 2-mercaptobenzothiazolates of trivalent lanthanides. Phys Chem Chem Phys 17:11000–11005. doi: 10.1039/C4CP05928J

20. Altun A, Kuliyev E, Aghatabay NM (2016) Tautomeric conversion, vibrational spectra, and density functional studies on peripheral sulfur derivatives of benzothiazole and benzothiazoline isomers. Spectrochim Acta Part A Mol Biomol Spectrosc 152:181–191. doi: 10.1016/j.saa.2015.07.071

21. Serdechnova M, Ivanov VL, Domingues MRM, et al. (2014) Photodegradation of 2-mercaptobenzothiazole and 1,2,3-benzotriazole corrosion inhibitors in aqueous solutions and organic solvents. Phys Chem Chem Phys 16:25152–25160. doi: 10.1039/C4CP03867C

22. Wang G, Harrison a, Li X, et al. (2004) Study of the adsorption of benzimidazole and 2-mercaptobenzothiazole on an iron surface by confocal micro-Raman spectroscopy. J Raman Spectrosc 35:1016–1022. doi: 10.1002/jrs.1235

23. Sandhyarani N, Skanth G, Berchmans S, et al. (1999) A Combined Surface-Enhanced Raman-X-Ray Photoelectron Spectroscopic Study of 2-mercaptobenzothiazole Monolayers on Polycrystalline Au and Ag Films. J Colloid Interface Sci 209:154–161. doi: 10.1006/jcis.1998.5882

24. Malouki MA, Richard C, Zertal A (2004) Photolysis of 2-mercaptobenzothiazole in aqueous medium: Laboratory and field experiments. J Photochem Photobiol A Chem 167:121–126. doi: 10.1016/j.jphotochem.2004.04.010

25. Masoud MS, Abou Ali SA, Ali GY, El-Dessouky MA (1983) Substituent effects on the dissociation constants and the strength of the hydrogen bond in some azo cresol compounds. J Chem Eng Data 28:297–300. doi: 10.1021/je00033a004

26. Isidro-Llobet A, Just-Baringo X, Ewenson A, et al. (2007) Fmoc-2-mercaptobenzothiazole, for the introduction of the Fmoc moiety free of side-reactions. Biopolymers 88:733–7. doi: 10.1002/bip.20732

27. Frisch MJ, Trucks GW, Schlegel HB, et al. (2009) Gaussian 09, Rev A.1. Gaussian Inc Wallingford CT

28. Zhao Y, Truhlar DG (2008) The M06 suite of density functionals for main group thermochemistry, thermochemical kinetics, noncovalent interactions, excited states, and transition elements: two new functionals and systematic testing of four M06-class functionals and 12 other function. Theor Chem Acc 120:215–241. doi: 10.1007/s00214-007-0310-x

29. Tomasi J, Mennucci B, Cammi R (2005) Quantum mechanical continuum solvation models. Chem Rev 105:2999–3093. doi: 10.1021/cr9904009

30. Scalmani G, Frisch MJ, Mennucci B, et al. (2006) Geometries and properties of excited states in the gas phase and in solution: theory and application of a time-dependent density functional theory polarizable continuum model. J Chem Phys 124:94107. doi: 10.1063/1.2173258

31. Becke AD (1993) Density-functional thermochemistry. III. The role of exact exchange. J Chem Phys 98:5648. doi: 10.1063/1.464913

32. Stanton JF, Bartlett RJ (1993) The equation of motion coupled-cluster method. A systematic biorthogonal approach to molecular excitation energies, transition probabilities, and excited state properties. J Chem Phys 98:7029. doi: 10.1063/1.464746

33. Kállay M, Gauss J (2004) Calculation of excited-state properties using general coupled-cluster and configuration-interaction models. J Chem Phys 121:9257–69. doi: 10.1063/1.1805494

34. Caricato M, Trucks GW, Frisch MJ, Wiberg KB (2010) Electronic transition energies: A study of the performance of a large range of single reference density functional and wave function methods on valence and rydberg states compared to experiment. J Chem Theory Comput 6:370–383. doi: 10.1021/ct9005129

35. Caricato M, Trucks GW, Frisch MJ, Wiberg KB (2011) Oscillator strength: How does TDDFT compare to EOM-CCSD? J Chem Theory Comput 7:456–466. doi: 10.1021/ct100662n

36. Caricato M (2012) Absorption and emission spectra of solvated molecules with the EOM-CCSD-PCM method. J Chem Theory Comput 8:4494–4502. doi: 10.1021/ct3006997

37. Boys SF, Bernardi F (1970) The calculation of small molecular interactions by the differences of separate total energies. Some procedures with reduced errors. Mol Phys 19:553–566. doi: 10.1080/00268977000101561

38. Simon S, Duran M, Dannenberg JJ (1996) How does basis set superposition error change the potential surfaces for hydrogen-bonded dimers? J Chem Phys 105:11024. doi: 10.1063/1.472902

39. Shields GC, Seybold PG (2013) Computational Approaches for the Prediction of pKa Values. CRC Press

40. McQuarrie DA, Simon JD (1997) Physical Chemistry: A Molecular Approach.

University Science Books

41. Palascak MW, Shields GC (2004) Accurate Experimental Values for the Free Energies of Hydration of H + , OH - , and H 3 O +. J Phys Chem A 108:3692–3694. doi: 10.1021/jp049914o

42. Chesick JP, Donohue J (1971) The molecular and crystal structure of 2-mercaptobenzothiazole. Acta Crystallogr Sect B Struct Crystallogr Cryst Chem 27:1441–1444. doi: 10.1107/S0567740871004102

43. Zhang J, Li F, Zhang R (2004) Syntheses and Crystal Structures of Benzyltin(IV) Derivatives of 2-Merpcatobenzothiazole. Chinese J Chem 22:2775–2783. doi: 10.1002/ejic.200300860

44. Bordwell FG (1988) Equilibrium Acidities in Dimethyl Sulfoxide Solution. Acc Chem Res 21:456–463. doi: 10.1021/ar00156a004

45. Poznański J, Najda A, Bretner M, Shugar D (2007) Experimental (13C NMR) and theoretical (ab Initio molecular orbital calculations) studies on the prototropic tautomerism of benzotriazole and some derivatives symmetrically substituted on the benzene ring. J Phys Chem A 111:6501–6509. doi: 10.1021/jp071611h

46. Houllihan WJ (1972) The Chemistry of Heterocyclic Compounds, Indoles Part One. Wiley-Interscience

47. Serjeant E (1979) Ionisation constants of organic acids in aqueous solution. Pergamon Press

48. Foulon C, Duhal N, Lacroix-Callens B, et al. (2007) Determination of pKa values of benzoxa-, benzothia- and benzoselena-zolinone derivatives by capillary electrophoresis. Comparison with potentiometric titration and spectrometric data. Eur J Pharm Sci 31:165–171. doi: 10.1016/j.ejps.2007.03.002

49. Irudayam SJ, Henchman RH (2009) Entropic cost of protein-ligand binding and its dependence on the entropy in solution. J Phys Chem B 113:5871–84. doi: 10.1021/jp809968p

50. (2001) Encyclopedia of Reagents for Organic Synthesis. John Wiley & Sons, Ltd

51. Golabi SM, Mohammadi J (2003) Wire-Coated Silver(I) Ion-Selective Electrode Based on 2-Mercaptobenzothiazole (MBT) Ionophore: Application to the Determination of Silver in Real Samples. Anal Sci 19:877–881. doi: 10.2116/analsci.19.877